Three-Dimensional Atom-Probe Tomographic Analyses of Lead-Telluride Based Thermoelectric Materials

YOON-JUN KIM,[1] IVAN D. BLUM,[1,4] JIAQING HE,[1,5]
MERCOURI G. KANATZIDIS,[2] VINAYAK P. DRAVID,[1]
and DAVID N. SEIDMAN[1,3,6]

1.—Department of Materials Science and Engineering, Northwestern University, 2220 Campus Drive, Evanston, IL 60208-3108, USA. 2.—Department of Chemistry, Northwestern University, 2145 Sheridan Road, Evanston, IL 60208-3113, USA. 3.—Northwestern Center for Atom-Probe Tomography, 2220 Campus Drive, Evanston, IL 60208-3108, USA. 4.—*Present address:* Groupe de Physique des Matériaux, UMR CNRS 6634, Normandie University, University of Rouen and INSA Rouen, 76801 St. Etienne du Rouvray, France. 5.—Department of Physics, South University of Science and Technology of China, Shenzhen 518055, People's Republic of China. 6.—e-mail: d-seidman@northwestern.edu

Precipitates in bulk p-type thermoelectric materials, PbTe-SrTe and PbTe-PbS, are studied using three-dimensional (3-D) atom-probe tomography (APT). APT is capable of characterizing chemically materials in 3-D with subnano-scale spatial resolution on an atom-by-atom basis, which enables us to characterize secondary phases in the PbTe matrix as well as the dopant distributions at different imperfections. We demonstrate that APT provides accurate information about the compositions and morphologies of nanoprecipitates. In the PbTe-SrTe system, different morphology of precipitates is observed and the SrTe composition is confirmed. Also, segregation of Na dopants at mesoscale imperfections, dislocations and grain boundaries, and at matrix/precipitate interfaces is observed. In the PbTe-PbS system, PbS precipitates are observed. The PbS precipitates exhibit faceting, and have a morphology that depends on the bulk Na concentration. A predominance of {100} faceted precipitates is observed for 2 mol.% Na. Using 3-D APT, we demonstrate that Na segregation at matrix/precipitate interfaces is most likely responsible for the change in their morphologies, which occurs by reducing the interfacial free energy of {100} facets.

INTRODUCTION

Thermoelectric materials can be used to convert heat to electrical energy and can also be used in applications such as waste heat recovery. The intrinsic efficiency of a thermoelectric material is defined by its figure of merit, $ZT = \sigma S^2/(\kappa_{el} + \kappa_{lat})$, where σ is the electrical conductivity, S is the seebeck coefficient, T is temperature in K, κ_{el} is the electronic thermal conductivity, and κ_{lat} is the lattice thermal conductivity.[1–4] This equation implies that an efficient thermoelectric material needs to have an optimal electrical conductivity, a high Seebeck coefficient and yet maintain a lattice thermal conductivity as small as possible: the ideal material would behave like a crystal for electrons, but like glass for phonons.[1] In this respect, PbTe has intrinsically good properties, but they must be improved to produce efficient devices. This desired result can be achieved through different strategies.[5] One of them is to decrease the lattice contribution to the thermal conductivity, κ_{lat}, by introducing nanostructures into a material.[6] For example, semi-coherent SrTe precipitates in a PbTe matrix, increase phonon scattering without any negative effects on the electrical conductivity.[7] This efficient strategy yields values of ZT of 1.7 at 800 K, which can be further improved. To further decrease κ_{lat}, it is necessary to have an excellent understanding of the effects of nanostructures on the thermoelectric properties of materials, as well as understanding and controlling their formation. This can only be achieved using powerful characterization methods. Three-dimensional (3-D) atom-probe tomography

(APT) is able to provide information on the chemical composition of a specimen on an atom-by-atom basis, in 3-D at the subnanometer scale.[8,9] It has already been proven to be extremely useful for understanding the formation of nanostructures in metallic alloys and semiconductors.[10] Its usefulness was also proven in the case of the system PbTe-Ag_2Te, where it enabled the characterization of the temporal evolution of precipitates in a PbTe matrix during aging.[11]

In this article, we demonstrate the contributions of 3-D APT to the understanding of the effect of nanostructures on the thermoelectric properties of PbTe-based materials, and to the understanding of the formation of these nanostructures in high ZT materials. In the case of the PbTe-SrTe system, thanks to sample preparation by spark plasma sintering, an additional decrease in κ_{lat} can be achieved by introducing mesoscale imperfections, specifically grain boundaries, which scatter phonons with long mean-free paths, which are not affected significantly by nanometer scale precipitates. This strategy allows achieving a value of ZT of 2.2 at 900 K.[12] For this system, we demonstrate that 3-D APT provides accurate information about the nanoprecipitates and the spatial distribution of dopants. We demonstrate that imperfections can serve as a reservoir for Na dopants that are released into the PbTe lattice at high temperatures, thereby increasing the high-temperature electrical conductivity, which contributes to the record ZT values that are measured. In another system, PbTe-PbS, where PbS precipitates are used to scatter phonons, we observe that the precipitates's morphologies are affected by different concentrations of Na dopants.[13] 3-D APT is utilized to demonstrate quantitatively that Na segregates at the precipitate/matrix interfaces. Our results demonstrate that interfacial Na segregation is most likely responsible for a change in the precipitate morphology by decreasing the interfacial free energy of {001} facets. We also demonstrate that sample preparation by slow cooling yields a nonequilibrium dopant distribution.

BACKGROUND

Three-Dimensional Atom-Probe Tomography

A major advantage of 3-D APT is that it permits a 3-D reconstruction of the lattice on an atom-by-atom basis, which permits one to obtain accurate chemical concentrations of all the elements in the periodic table with essentially the same detection efficiency. The 3-D atomic scale reconstruction of a sample is obtained by combining the times-of-flights (TOFs) and the x-, y-, and z-positional data of all the evaporated atoms in an analyzed volume with subnanoscale spatial resolution. Additionally, TOF mass spectra, based on mass-to-charge state (m/n) ratios, are utilized to obtain quantitative chemical analyses of the 3-D reconstructed sample.

Figure 1 is a schematic diagram of the local-electrode atom-probe (LEAP) tomograph[8] utilized in this study, which we call an APT for brevity. An array of microtip specimens sits on an electrically conducting substrate, Si in general, at a DC voltage of V_{dc}. To evaporate atoms as ions, the local-electrode, which is conically shaped with a 30-μm diameter orifice, is placed within about 30 μm of the apex of a microtip specimen. The average electric field (E) at the apex of a microtip is given by:

$$E = \frac{V_{dc}}{kR};$$ (1)

where V_{dc} is the applied DC voltage, k is a shape dependent factor ($\sim$3.3), and R is the microtip's mean radius. For electrically conducting specimens, such as metals, the evaporation can be triggered by applying an electrical pulse with a negative potential, V_{pulse}, applied to the local-electrode, which increases the local E-field at a microtip to the requisite value; a typical pulse fraction, V_{pulse}/V_{dc}, is 0.15–0.25. In the case of semiconducting or insulating specimens, the evaporation of atoms as ions is triggered by applying a laser pulse to the apex of the microtip.[8,14–16] The transient increase in temperature caused by the laser beams results in evaporation of ions in the presence of the applied DC voltage. The position-sensitive detector utilized consists of an 80-mm diameter multichannel plate (MCP) in series with a delay-line detector at a typical distance of 90 mm from a microtip. The MCP plus a delay-line detector measures an ion's TOF and its positional coordinates within an atomic plane: the spatial accuracy of the delay-line detector is < 0.2 mm, with a timing accuracy of 50 ps and a multihit resolution of 1.5 ns.[17] Employing electrical pulses, the pulse repetition rate is variable in discrete steps from 1 kHz to 250 kHz at a detection rate of up to 2×10^6 ions min^{-1}. The field-evaporated ions hitting a MCP detector with different mass-to-charge state ratios (m/n) are used to reconstruct a 3-D image of a microtip using Eq. 2.

$$\frac{m}{n} = 2eV_{dc}\frac{t^2}{d^2};$$ (2)

where e is the charge on an electron, V_{dc} is the DC voltage, d is the measured flight distance of an pulse evaporated ion, and t is an ion's measured time-of-flight (TOF) corrected for the propagation time in the cables.

A 3-D APT tomograph can also be operated utilizing a pulsed ultraviolet (UV) picosecond laser (wavelength = 335 nm) to evaporate atoms from a sharply pointed needle-like microtip as ions or molecules.[8,14–16] When used with UV laser pulsing, the pulse repetition rate is variable from 1 kHz to 1000 kHz, with a detection rate of up to 5×10^6 ions min^{-1} for a user friendly microtip, that is, one that does not fracture readily: fracture of a microip occurs less frequently with UV laser pulsing
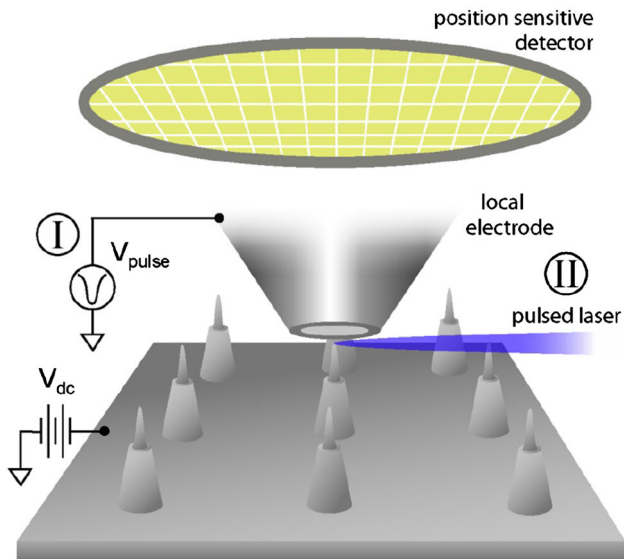
Fig. 1. Schematic of a local-electrode atom-probe (LEAP) tomograph employing either voltage, I, or laser pulses, II. The substrate, which contains an array of microtip specimens, is maintained at a positive potential, V_{dc}; the substrate can be translated in the x–y plane. The local-electrode is pulsed with a negative voltage, V_{pulse}, to increase the E-field at a microtip specimen to the requisite value for field evaporating atoms as ions. Alternatively, a specimen is pulsed with picosecond laser pulses at a high repetition rate. II—Ultraviolet laser light (wavelength = 355 nm).[8]

than it does with voltage pulsing because the concomitant Maxwell elastic stresses exerted on a microtip are significantly smaller. The UV laser's key variable parameters are energy pulse^{-1}, pulse duration, and pulse repetition rate. For either electrical or laser pulsing, the cross-sectional area of an analyzed microtip can be 200×200 nm^2 at a TOF distance of 90 mm. The depth to which a microtip can be analyzed is material dependent and may be 1-μm or greater. The detection sensitivity for all elements is about 10 atomic parts per million for an UV laser under ultrahigh vacuum conditions, $<10^{-10}$ Torr.

EXPERIMENTS

Specimen Preparation

A dual-beam focused-ion beam (FIB) microscope (FEI Helios Nanolab, Hillsboro, OR, USA) is used to prepare microtip samples for APT analysis. Dual-beam FIB microscopy[18] and its application to the fabrication of APT microtip specimens has improved dramatically the ability to prepare microtips of different materials in different configurations. This methodology relies on using low-energy (30 kV to 2 kV) Ga$^+$ ions to sputter material with a high accuracy in a specified region,[19] so that a microtip can be fabricated to contain a desired nanostructural feature, for example, a precipitate or a grain boundary. A more exhaustive description of the different specimen preparation techniques is described elsewhere.[20]

Figure 2 displays the procedure utilized to prepare APT specimens from PbTe-based thermoelectric materials. The following steps are employed: (1) Pt deposition on a piece of thermoelectric material to protect it from Ga$^+$ ion damage; (2) a trench is cut to produce a long specimen with a triangular-shaped cross-section; (3) the long specimen is lifted-out using a micromanipulator; (4) the long specimen is transferred to a Si micropost, with a flat top, sitting on a coupon; (5) it is then cold-welded to the Si micropost using Pt; (6) the Ga$^+$ ion beam is used to separate the long specimen, leaving behind a small specimen, with a triangular cross-section, sitting on a Si micropost; (7) the Ga$^+$ ion beam is used to form the short specimen into a conically shaped specimen; and (8) and (9) it is finally shaped into a sharply pointed microtip with a radius of curvature of <50 nm.

Atom-Probe Tomographic Analysis

The 3-D APT (Cameca LEAP-4000X Si, Madison, WI, USA) is equipped with a picosecond UV laser (wavelength = 355 nm). During the analysis of samples of the PbTe-PbS system, the sample was maintained at 32.4 K, a laser energy of 20 pJ pulse^{-1} was employed at a pulse repetition rate of 250 kHz, utilizing a target evaporation rate of 0.02 atom pulse^{-1}. Samples of the PbTe-SrTe system were analyzed using the voltage pulsing mode, with an evaporation rate of 0.005 atom pulse^{-1}, a pulse fraction (ratio of pulsed voltage to steady-state dc voltage) of 0.15, and a pulse repetition rate of 200 kHz. Individual ions were detected using a two-dimensional microchannel plate detector with detection efficiency of 50%. The data collected were analyzed using the program IVAS, v.3.6.6 (Cameca, Madison, WI, USA).

RESULTS AND DISCUSSION

PbTe-SrTe System

The maximum achievable ZT values for the Na doped PbTe–SrTe system is dependent on its atomic and nano-/micro-structure (Fig. 3a).[12] Combining the effects of atomic-scale alloy doping, endotaxial nanostructuring (precipitation) and mesoscale grain-boundary control, maximum phonon scattering can be achieved at high temperatures and ZT can be improved beyond what is achievable by nanostructuring alone. For instance, substitution of atomic-scale dopants into PbTe in a 2 mol.% Na–PbTe bulk ingot can lead to a ZT value of approximately 1.1 at 775 K. The ZT maximum value increases to ~1.7 at 800 K (Fig. 3b) by formation of SrTe nanoprecipitates with diameters of 2–10 nm in the Na-doped PbTe matrix.[7] Improvement of ZT is driven by the fact that the nanostructures impede much of the heat flow in this system, while the hole mobility remains largely unaffected.[7] The nanostructure in the bulk PbTe matrix scatters short-
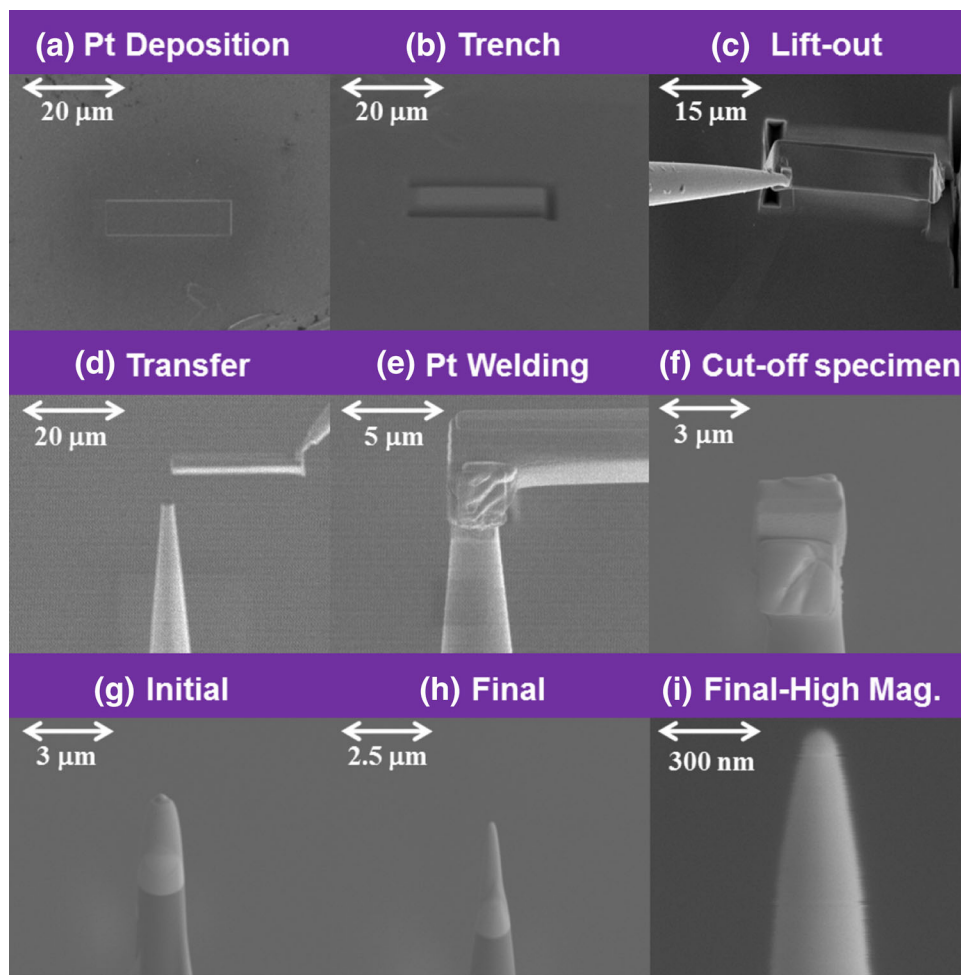
Fig. 2. Procedure used to prepare atom-probe tomographic microtips from bulk thermoelectric material using a Helios dual-beam focused-ion beam (FIB) microscope: note the different length scales at the different stages of microtip specimen preparation.

and medium- mean-free path phonons in the range from 3 nm to 100 nm, but it does not affect longer mean-free path phonons. The longer mean-free path phonons range from 0.1 μm to 1 μm, which are scattered by additional features of the mesoscale structure, such as grain boundary scattering and acoustic impedance mismatch at heterophase interfaces.

The contributions of phonons with different mean-free paths on the accumulated percentage of κ_{lat} have recently been calculated for PbTe (Fig. 4).[21,22] Approximately ~80% of κ_{lat} of PbTe is contributed by phonons having mean-free paths less than 100 nm, which can be attributed to scattering by atomic-scale solid-solution solute atoms and nanoscale precipitates in the PbTe matrix (Fig. 4).[21,23] The remaining ~20% of κ_{lat} of PbTe is, however, contributed by phonon modes with mean-free paths in the range 0.1–1 μm. In our research, samples were prepared as powders and processed using spark plasma sintering (SPS) instead of slow cooling (more details about the sample preparation methods are found elsewhere[12]); the smaller

thermal budget allows the formation of smaller grains, and hence a larger area per unit volume of grain boundaries. These mesoscale grain boundaries are comparable to the phonons with a mean free path of ~0.1–1 μm and they can scatter a significant fraction of the additional longer mean-free path heat carrying phonons. This results in a further reduction of κ_{lat} compared to nanostructuring alone.[8]

Scanning transmission electron microscopy (STEM) investigations were performed to obtain clear structural and compositional information of the nanoscale precipitates. Figure 5a displays a STEM micrograph exhibiting the presence of nanoprecipitates in conjunction with energy dispersive x-ray spectroscopy (EDS) results, which also exhibit a Sr signal from the precipitates (black), without a Sr peak from the matrix regions (blue). Therefore, qualitatively, the precipitates consist of mainly SrTe (see inset in Fig. 5a).[8]

Quantitative compositional analyses of SrTe nanoscale precipitates in the PbTe matrix are possible utilizing 3-D APT.[16] The 3-D reconstruction of
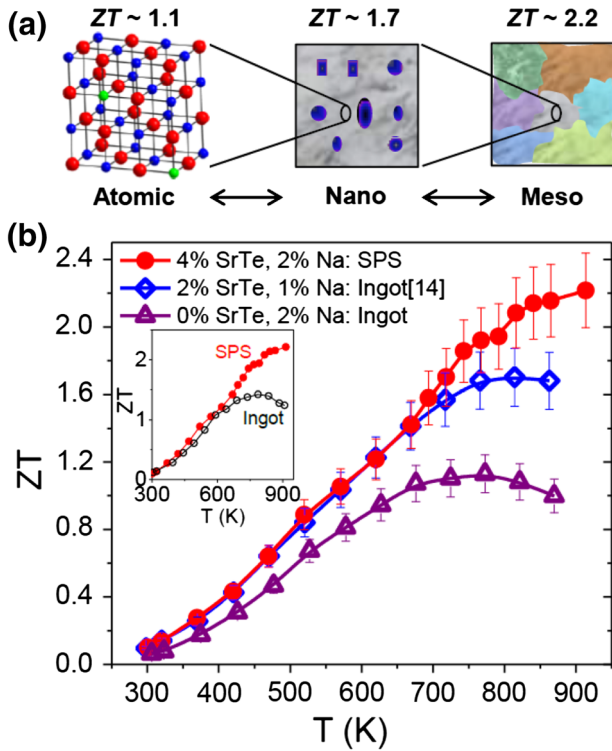
Fig. 3. (a) Maximum achievable ZT values with increasing length scale from scattering by atoms to mesoscale scattering. Red, Te; blue, Pb; and green dopant atoms are indicated in the atomic-scale structure. (b) ZT as a function of temperature for an ingot of PbTe doped with 2 mol.% Na (atomic-scale), PbTe-2 mol.% SrTe doped with 1 mol.% Na (atomic plus nanoscale) and spark plasma sintered (SPS) PbTe-4 mol.% SrTe specimen doped with 2 mol.% Na (atomic plus nano plus mesoscale). Inset in (b) is a comparison of ZT between a SPS specimen and an ingot sample with same composition of PbTe-4 mol.% SrTe doped with 2 mol.% Na[12] (Color figure online).
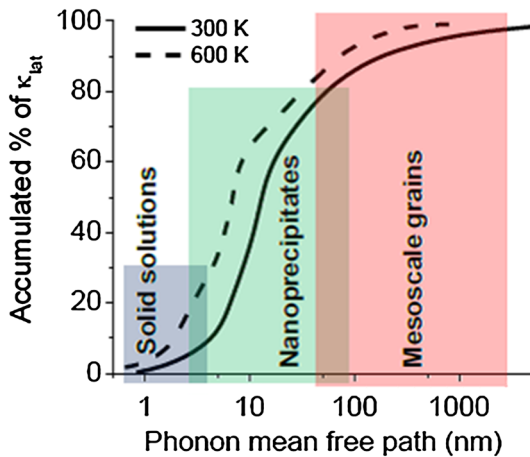

Fig. 4. Contributions of different mean free path phonons on the accumulated percentage of the lattice thermal conductivity, κ_{lat}, for PbTe.[21] Short, medium and long mean free path phonons can be scattered by atomic-scale defects, nanoscale precipitates, and mesoscale grain boundaries, respectively.[12,23]

the volume analyzed by APT for the PbTe–4 mol.% SrTe sample doped with 2 mol.% Na is displayed in Fig. 5b. The large SrTe precipitate has a diameter and morphology similar to that observed by STEM (Fig. 5a). Strontium-rich precipitates are highlighted by a pink 25 at.% Sr isoconcentration surface. The compositions of both the PbTe matrix and SrTe precipitates are listed in Table I. The concentration profile across the interface of the large precipitate is measured using a proximity histogram (Fig. 5c), which indicates that Na accumulates at the interface to a maximum concentration of 1.6 at.% Na. Additionally, Fig. 5c also exhibits a slight concentration gradient in the matrix with a smaller Na concentration near the interface than in the matrix. Sodium atoms also segregate at the cores of dislocations and grain boundaries in the same 3-D reconstructed volume (Figs. 5d and 6).

Segregated Na atoms will re-dissolve in the PbTe matrix at elevated temperatures because they are bound by an attractive binding enthalpy that appears in a Boltzmann factor, which decreases with increasing temperature. The net effect is to increase the p-type charge carrier density, which enhances the electrical conductivity of PbTe doped with Na. The existence of Na-rich precipitates had been reported from their presence in as cast ingots using TEM/EDS.[24] Clustering of Na atoms was also observed using 3-D APT.[25] If Na clusters are also present in the present sample, their dissolution at elevated temperature would also cause an increase in the electrical conductivity.

PbTe-PbS System

In this system, phonon scattering is caused by PbS precipitates, while Na is used for doping. The PbTe-PbS system with concentrations at and below PbTe–12 mol.% PbS–2 mol.% Na exhibit marked improvements in ZT with the highest ZT of 1.8 at 800 K.[26] Introducing PbS into 2 mol.% Na-doped PbTe significantly decreases the power factor, especially for more than 12 mol.% of PbS compared to its PbTe-based counterparts, because the heavy hole band lies much lower in energy relative to the light hole valence band and does not contribute to the charge transport properties. The total thermal conductivity of the PbTe-PbS system is, however, reduced over the entire temperature range in comparison to that of PbTe.

The ZT performance of the PbTe-PbS-Na system is correlated with nanostructure formations. Change of PbS precipitate morphology by the presence of a third element (dopant), Na, has been reported in this system. Major findings are that Na has a much greater solid-solubility in PbS than in PbTe, and it partitions into the PbS precipitates across PbTe/PbS interfaces. TEM analyses have shown that the precipitates are semi-coherent and are faceted.[13] Additionally, significant segregation
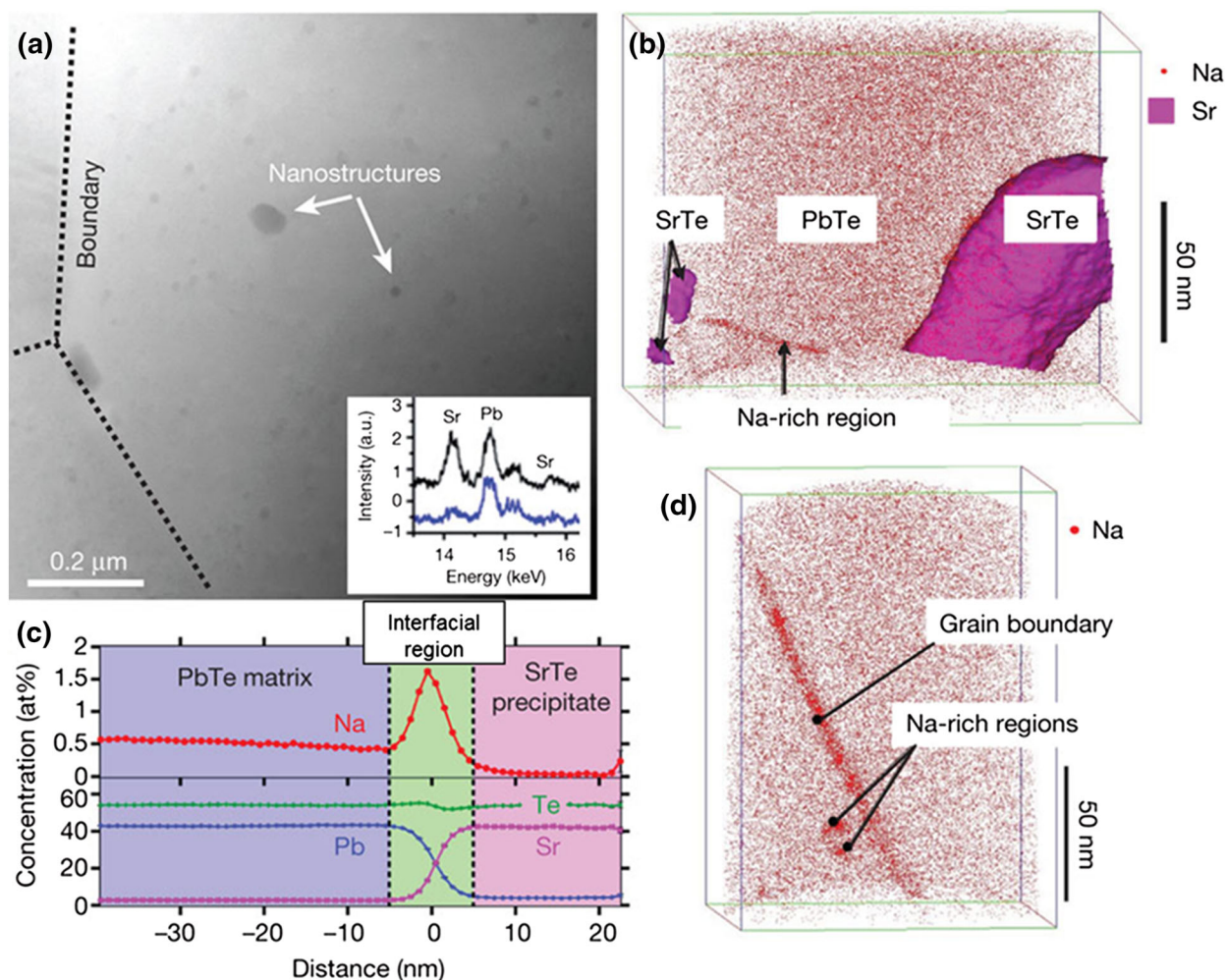
Fig. 5. Compositional analyses of PbTe-4 mol.% SrTe doped with 2 mol.% Na. (a) scanning transmission electron microscope image of SrTe precipitates in a PbTe matrix. Inset in (a) shows an energy dispersive spectrum (black precipitate and blue matrix). (b) Three-dimensional reconstruction of the volume analyzed by atom-probe tomography (SrTe precipitates highlighted using a 25 at.% Sr isoconcentration surface). (c) Proximity histogram showing the concentration profiles of Pb, Te, Sr and Na across the interface of a large SrTe precipitate. (d) Three-dimensional reconstruction displaying only Na atoms in the volume analyzed volume by atom-probe tomography, which contains a grain boundary[12] (Color figure online).

Table I. Precipitate and matrix compositions in a PbTe-SrTe-Na specimen analyzed by atom-probe tomography far from the precipitate's interface as displayed in Fig. 5b

Elements	Matrix (at.%)	Precipitate (at.%)
Pb	42.30 ± 0.01	3.70 ± 0.01
Te	54.18 ± 0.01	53.50 ± 0.01
Sr	2.85 ± 0.01	42.76 ± 0.01
Na	0.67 ± 0.01	0.04 ± 0.01

The experimental errors were calculated using counting statistics.

of Na at PbTe-matrix/PbS-precipitate interfaces result in highly faceted morphologies, implying an anisotropy of the interfacial free energy caused by Na segregation. Morphological control is also

governed by the ratio of PbS to Na concentrations and by the thermal processing procedure utilized. These findings have significant implications for the temporal evolution of the anisotropic morphology in precipitate/matrix systems (for example, as occurs in metallic alloys), such as PbTe/PbS-Na, and also for understanding and controlling the transport properties of nanostructured thermoelectric systems.[26]

To understand the formation mechanism of faceted precipitates, correlative analyses using HRTEM imaging (Fig. 7) and 3-D APT (Fig. 8) were performed. Samples in this study were prepared as cast ingots, simply by mixing the different elements and melting and slow cooling them under vacuum during 3 h. More details about sample preparation can be found elsewhere.[26] The TEM observations demonstrate that precipitates with rectangular cross-sections form facets parallel to the {100}
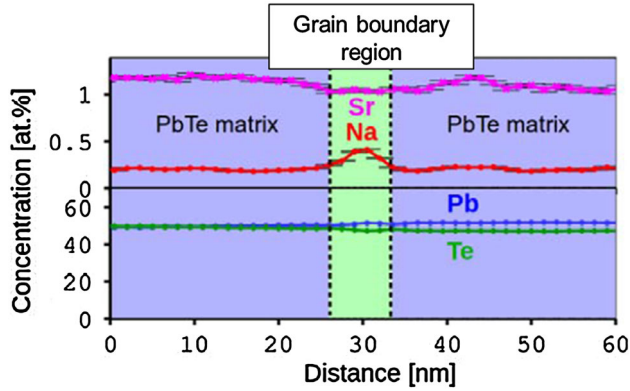
Fig. 6. Concentration profiles measured utilizing atom-probe tomography perpendicular to a grain boundary in a volume containing the entire grain boundary, which is indicated in Fig. 5d.

planes, while the precipitates with hexagonal cross-sections exhibit facets parallel to {111} and {100} planes and a very few display {110} facets. Figure 7 shows three typical morphologies of the PbS precipitates when using the [100] zone axis of PbTe in the 1 mol.% Na-doped PbTe-12 mol.% PbS sample. Figure 7a displays a precipitate with a square cross-section projected along the [100] zone axis with all edges along the [001] and [010] directions. The Moiré fringes in the precipitate are due to matrix/precipitate overlap along the viewing direction. One corner of the precipitate (Fig. 7b) appears to be cut along the [011] direction, and the same feature is observed for the four corners of the rectangular precipitate displayed (Fig. 7c). A careful examination of the precipitate in Figs. 7c and 8, demonstrates that what appears to be a (011) facet is the projection of a (111) facet along the [100] direction. The presence of a (111) facet is confirmed by the gradually increasing contrast along the [011] direction, while the contrast is sharp along the (001) PbTe/PbS interface, indicating an inclined surface of a PbS precipitate with respect to the PbTe matrix. The schematic diagrams of 3-D precipitates exhibiting three different morphologies: a cube, a partially truncated cube, and a fully truncated cube are inserted into the respective images. Each TEM image was taken along the directions of the indicated black arrows in the schematic diagram of the 3-D precipitates.

Since EDS and electron energy-loss spectroscopy analyses in the TEM did not detect significant differences between the interfacial and precipitate compositions, due to their limited sensitivities, 3-D APT is utilized for quantitative composition analyses of the interfacial regions. Analyses of the 1 mol.% Na doped PbTe-12 mol.% PbS sample by 3-D APT exhibits evaporation of both atoms and molecules: specifically, Na^+, S^+, S^{2+}, Te^+, Te^{2+}, Te_2^+, Te_2^{2+}, Pb^+, Pb^{2+}, $PbTe^+$, PbS^+, and $PbTe^{2+}$. Among these ions, Te^+ and Te_2^{2+} have similar mass-to-charge state (m/n) ratios, and thus they exhibit several overlapping peaks in the mass spectra. The contribution of each ion to the overall composition was measured by deconvoluting the corresponding peaks using a fitting procedure.[11] The presence of a portion of a sulfur-rich precipitate appears in a 3-D reconstruction (Fig. 8a). Utilizing a 25 at.% S isoconcentration surface in the analyzed volume yields the morphology of the PbS precipitate, which is consistent with a truncated cube having two types of facets. The large facets are parallel to {100} planes, while the smaller facets are parallel to {111} planes, confirming the TEM observations, Fig. 7c. A large facet implies a small interfacial free energy, while a small facet implies a large interfacial free energy.

The measured compositions of the matrix and precipitate by 3-D APT are listed in Table II, and the measured PbTe and PbS compositions are close to the nominal compositions for the matrix and precipitate. Additionally, the Na dopant has a higher concentration in the PbS precipitate than in the PbTe matrix. The Na concentration is 3.49 at.% in the precipitate, while it is only 0.33 at.% in the matrix. The resulting partitioning coefficient of Na between the two phases, ($PbS^{Na}/PbTe^{Na}$), is 10.6 indicating that Na atoms are more soluble in the PbS precipitate than in the PbTe matrix. Figure 9 displays the concentration profiles perpendicular to the (100) facet (Fig. 7b) and to the (111) facet (Fig. 7c). In the case of the (100) interface, Na segregates at a maximum concentration of 5 at.%.

Na segregation at the precipitates' interfaces is quantified by the relative Gibbsian interfacial excess, which represents the excess number of solute atoms per unit area of interface compared to the number of atoms that would be present in the absence of segregation. 3-D APT is the only direct method capable of measuring this quantity quantitatively for interfaces in the solid-state.[27] We employed the formalism developed by Cahn[28,29] to calculate the interfacial excess, which involves placing two surfaces that straddle the interface in regions where there isn't a concentration gradient, between which the number of atoms of each species is counted. In Cahn's formalism the Gibbsian interfacial excess of Na with respect to Te and S is given by:

$$\Gamma_{\text{Na}}^{\text{Te,S}} = N_{\text{Na}} - \frac{N_{\text{Te}}(X_{\text{Na}}^{\text{PbTe}}X_{\text{S}}^{\text{PbS}} - X_{\text{Na}}^{\text{PbS}}X_{\text{S}}^{\text{PbTe}}) - N_{\text{S}}(X_{\text{Na}}^{\text{PbTe}}X_{\text{Te}}^{\text{PbS}} - X_{\text{Na}}^{\text{PbS}}X_{\text{Te}}^{\text{PbTe}})}{X_{\text{Te}}^{\text{PbTe}}X_{\text{S}}^{\text{PbS}} - X_{\text{Te}}^{\text{PbS}}X_{\text{S}}^{\text{PbTe}}} \tag{3}$$
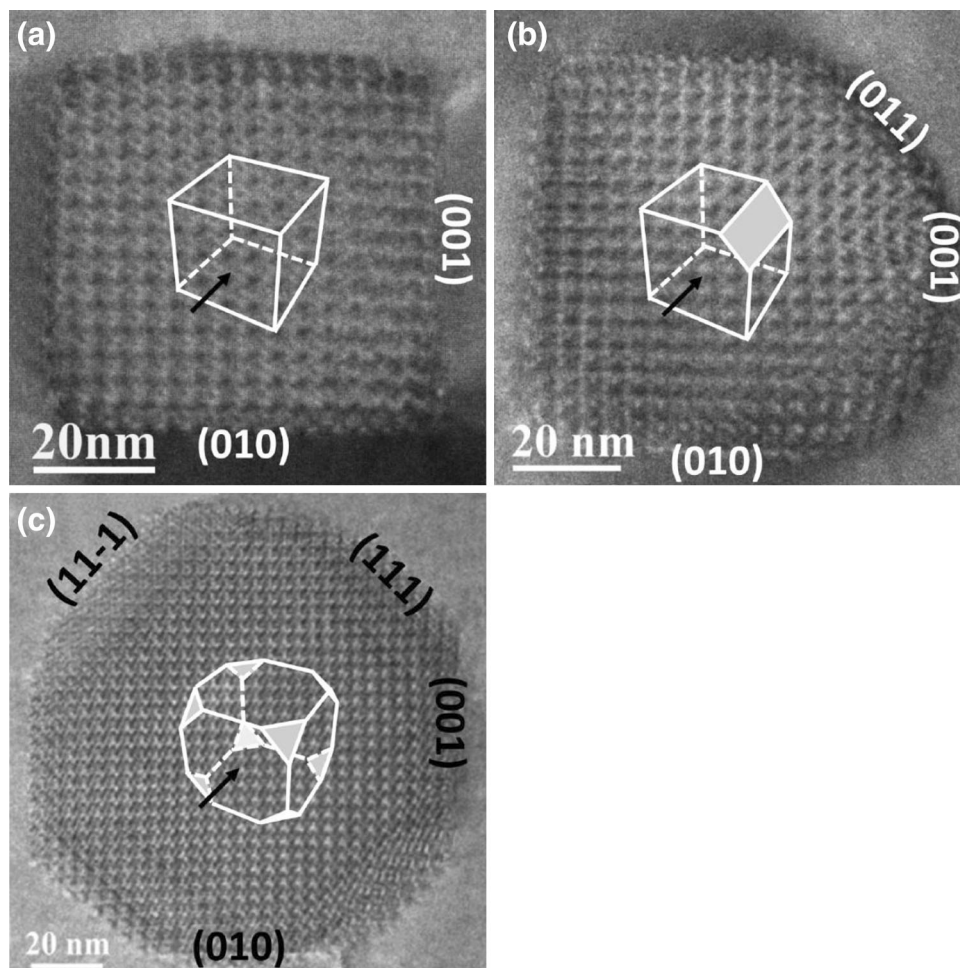
Fig. 7. HRTEM images of a 1 mol.% Na doped PbTe-PbS 12 mol.% sample displaying the three primitive projections of PbS precipitates. Schematic diagrams of the corresponding precipitate morphology in three-dimensinal space are inserted in (a), (b) and (c); the black arrowheads indicate the directions of the HRTEM observations.[13]
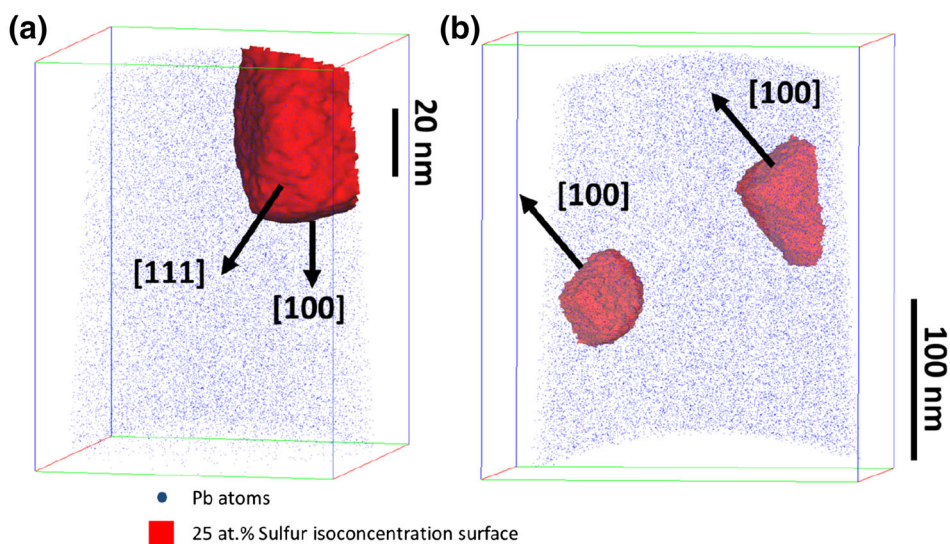

Fig. 8. Reconstructions of volumes of material analyzed by atom-probe tomography in the case of PbTe-12 mol.% PbS doped with (a) 1 mol.% Na and (b) 2 mol.% Na. The red surfaces are isoconcentration surfaces corresponding to a 25 at.% sulfur concentration and highlight the precipitates' interfaces. Only 1% of the Pb atoms are represented for clarity[13] (Color figure online).

Table II. Compositions of the matrix and a precipitate in the PbTe-PbS-Na system analyzed using atom-probe tomography

Elements	Matrix (at.%)	Precipitate (at.%)
Pb	48.42 ± 0.005	47.53 ± 0.13
Te	47.85 ± 0.005	Not detectable
S	3.39 ± 0.002	48.98 ± 0.13
Na	0.33 ± 0.001	3.49 ± 0.5
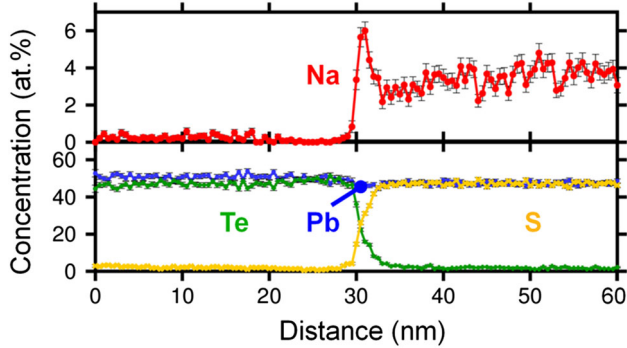
Fig. 9. Concentration profiles measured through a PbTe (001)/PbS interface for a PbTe-12 mol.% PbS-1 mol.% Na specimen.[13]

Table III. Interfacial excesses measured at (001) and (111) interfaces in a PbTe-12 mol.% PbS-1 and 2 mol.% Na specimen by atom-probe tomography

	Na interfacial excess (nm^{-2})	
Na nominal concentration	(001)	(111)
1 mol.% Na	3.79 ± 0.30	3.03 ± 0.47
	2.18 ± 0.29	2.15 ± 0.60
	1.19 ± 0.27	4.38 ± 0.60
2 mol.% Na	1.36 ± 0.29	–
	4.06 ± 0.27	–

where X_{ij} is the atomic fraction of i in phase j, measured in the vicinity of the interface and Ni is the number of atoms i counted in the region defined by the two surfaces straddling the interface. The result is then corrected for the detection efficiency of the 3-D APT, which is 50%. The interfacial excesses measured at the different facets for the two compositions are given in Table III. There are large differences between the excesses measured at the different facets, independent of their crystallographic orientation and even independent of the nominal Na concentration. The measured values are, however, all significant. As an example, the minimum measured excess is measured for a (001) facet, 1.19 ± 0.27 nm^{-2}, and the maximum excess is measured for a (111) facet, 4.38 ± 0.60 nm^{-2}; to

both the (001) and (111) facets in the case of the sample containing 1 mol.% Na (the uncertainties correspond to one sigma). For comparison, the atomic densities of the (100) and (111) PbTe planes are 9.64 and 5.57 atoms nm^{-2}, respectively. When projected onto a unique {hkl} plane, these two extreme values correspond to coverages of $12 \pm 3\%$ and $79 \pm 11\%$ of the (100) and (111) planes of PbTe, respectively. The large differences in measured excesses at the different facets show that the sample did not reach equilibrium. This could be explained by the fact that the sample was prepared by slow cooling (cooled over 3 h), and could not achieve equilibrium as during an isothermal heat treatment followed by a rapid quench. The Gibbs adsorption isotherm implies that the thermodynamic driving force for segregation is the reduction in the interfacial free energy. And different Gibbsian excesses at different {hkl} facets tell us that the interfacial free energies have been reduced by different amounts for different facets.

CONCLUSION

3-D APT analyses are utilized for characterizing PbTe-based thermoelectric materials. The subnanometer spatial resolution and atomic scale chemical information obtained from 3-D APT enables us to measure the chemical compositions of nanoscale precipitates, and study dopant distributions at different imperfections, dislocations and grain boundaries, as well as studying the temporal evolution of the precipitate morphology in 3-D.

3-D APT analyses of the *p*-type PbTe–SrTe system illustrate clearly segregation of Na dopants at mesoscale grain boundaries and PbTe/SrTe interfaces. Mesoscale phonon scattering plays a synergestic effect with nanoscale scattering by decreasing κ_{lat} to levels well beyond what endotaxial nanostructuring (precipitation) alone can achieve.

Using 3-D APT, we also observed Na segregation at different imperfections. Sodium is bound at these imperfections with an attractive binding free energy, which appears in a Boltzmann factor, and at high temperatures Na atoms are released, thereby increasing the electrical conductivity, which contributes to the high measured value of $ZT \sim 2.2$ at 915 K.

The PbS precipitate morphology in the PbTe matrix is controlled by the concentration ratio PbS to Na. This is likely a new strategy to control nanostructure morphology in (pseudo) binary systems; that is, by the partitioning of a ternary addition in a nominally binary system. 3-D APT enables us to quantify segregation of Na at the different facets of the PbS precipitates. We demonstrate that this segregation is significant and is most likely responsible for the change in the equilibrium morphology of the precipitates by reducing the interfacial free energy of {001} facets with respect to {111} facets.

ACKNOWLEDGEMENTS

REFERENCES

1. D.M. Rowe, *CRC Handbook of Thermoelectrics: Macro to Nano* (Boca Raton, FL: CRC Press, 2006).
2. T. Tritt, *Recent Trends in Thermoelectric Materials Research, Part One* (San Diego: Academic Press, 2000).
3. T. Tritt, *Recent Trends in Thermoelectric Materials Research, Part Two* (San Diego: Academic Press, 2000).
4. T. Tritt, *Recent Trends in Thermoelectric Materials Research: Part Three* (San Diego: Academic Press, 2001).
5. G.J. Snyder and E.S. Toberer, *Nat. Mater.* 7, 105 (2008).
6. M.G. Kanatzidis, *Chem. Mater.* 22, 648 (2009).
7. K. Biswas, J.Q. He, Q.C. Zhang, G.Y. Wang, C. Uher, V.P. Dravid, and M.G. Kanatzidis, *Nat. Chem.* 3, 160 (2011).
8. D.N. Seidman and K. Stiller, *MRS Bull.* 34, 717 (2009).
9. D. Blavette, A. Bostel, J.M. Sarrau, B. Deconihout, and A. Menand, *Nature* 363, 432 (1993).
10. T.F. Kelly and D.J. Larson, *Annu. Rev. Mater. Res.* 42, 1 (2012).
11. J.L. Lensch-Falk, J.D. Sugar, M.A. Hekmaty, and D.L. Medlin, *J. Alloy. Compd.* 504, 37 (2010).
12. K. Biswas, J.Q. He, I.D. Blum, C.I. Wu, T.P. Hogan, D.N. Seidman, V.P. Dravid, and M.G. Kanatzidis, *Nature* 489, 414 (2012).
13. J.Q. He, I.D. Blum, H.-Q. Wang, S.N. Girard, J. Doak, L.-D. Zhao, J.-C. Zheng, G. Casillas, C. Wolverton, M. Jose-Yacaman, D.N. Seidman, M.G. Kanatzidis, and V.P. Dravid, *Nano Lett.* 12, 5979 (2012).
14. M.K. Miller, *Atom Probe Tomography: Analysis at the Atomic Level* (New York: Kluwer Academic/Plenum Publishers, 2000).
15. A. Cerezo, T.J. Godfrey, S.J. Sijbrandij, G.D.W. Smith, and P.J. Warren, *Rev. Sci. Instrum.* 69, 49 (1998).
16. D.N. Seidman, *Annu. Rev. Mater. Res.* 37, 127 (2007).
17. G. Da Costa, F. Vurpillot, A. Bostel, M. Bouet, and B. Deconihout, *Rev. Sci. Instrum.* 76, 013304 (2005).
18. L.A. Giannuzzi and F.A. Stevie, *Micron* 30, 197 (1999).
19. D.J. Larson, D.T. Foord, A.K. Petford-Long, H. Liew, M.G. Blamire, A. Cerezo, and G.D.W. Smith, *Ultramicroscopy* 79, 287 (1999).
20. M.K. Miller, K.F. Russell, K. Thompson, R. Alvis, and D.J. Larson, *Microsc. Microanal.* 13, 428 (2007).
21. B. Qiu, H. Bao, G.Q. Zhang, Y. Wu, and X.L. Ruan, *Comp. Mater. Sci.* 53, 278 (2012).
22. Z.T. Tian, J. Garg, K. Esfarjani, T. Shiga, J. Shiomi, and G. Chen, *Phys. Rev. B* 85, 184303 (2012).
23. J. He, M.G. Kanatzidis, and V.P. Dravid, *Mater. Today* 16, 166 (2013).
24. J. He, J. Androulakis, M.G. Kanatzidis, and V.P. Dravid, *Nano Lett.* 12, 343 (2012).
25. I.D. Blum, D. Isheim, D.N. Seidman, J.Q. He, J. Androulakis, K. Biswas, V.P. Dravid, and M.G. Kanatzidis, *J. Electron. Mater.* 41, 1583 (2012).
26. S.N. Girard, J.Q. He, X.Y. Zhou, D. Shoemaker, C.M. Jaworski, C. Uher, V.P. Dravid, J.P. Heremans, and M.G. Kanatzidis, *J. Am. Chem. Soc.* 133, 16588 (2011).
27. S.A. Dregia and P. Wynblatt, *Acta Metall. Mater.* 39, 771 (1991).
28. A.P. Sutton and R.W. Balluffi, *Interfaces in Crystalline Materials* (Oxford: Clarendon Press, 1995).
29. J.W. Cahn, *Thermodynamics of Solid and Fluid Surfaces* (Metals Park: American Society for Metals, Materials Science Division, 1979).